ACS APPLIED NANO MATERIALS

Mixed-Metal 2D Chalcogenides $Mo_xRe_{1-x}S_2$ as Antifungal Near-Infrared-Responsive Nanozymes

Fei Zhang, Rishabh Sahani, Changliang An, Ha Na, Samuel A. Oyon, Daniela Radu, Anthony J. McGoron, and Cheng-Yu Lai*

Cite This: *ACS Appl. Nano Mater.* 2024, 7, 27717−27727

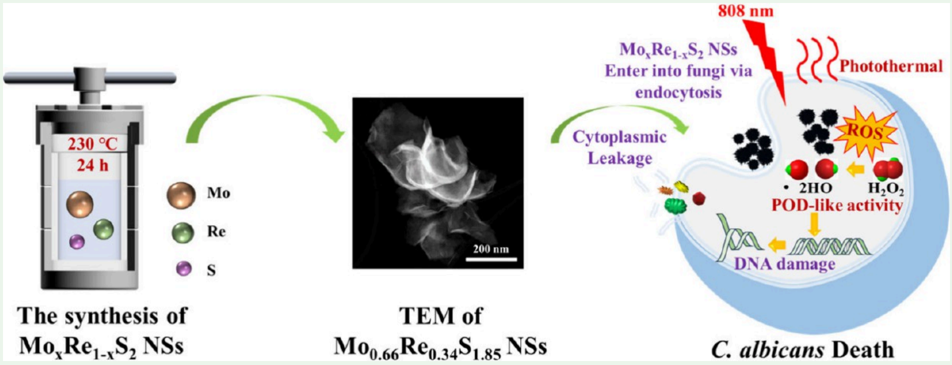

ABSTRACT: Nanozymes have emerged as a promising class of antimicrobial agents due to their broad-spectrum activity and negligible biotoxicity profiles. In recent years, transition metal dichalcogenides (TMDCs) have garnered significant attention for their diverse enzymatic properties, opening avenues for research and applications in various fields. Notably, the design of efficient multifunctional nanozymes based on TMDCs has emerged as a highly promising strategy for the treatment of fungal infections. Herein, $Mo_xRe_{1-x}S_2$ mixed-metal transition metal chalcogenides with tuned composition have been successfully synthesized by a hydrothermal method and tested for their nanozyme properties. Antifungal activities of $Mo_{0.66}Re_{0.34}S_{1.85}$ and $Mo_{0.81}Re_{0.19}S_{1.76}$ nanozymes were observed by scanning electron microscopy (SEM) showing that the fungal skeletal structure was either significantly deformed or completely collapsed. The $Mo_{0.66}Re_{0.34}S_{1.85}$ and $Mo_{0.81}Re_{0.19}S_{1.76}$ antifungal activities were also tested under 808 nm near-infrared (NIR) irradiation, showing photothermal enhancement. This work demonstrates temperature-augmented functional nanozymes for synergistic photothermal/biochemical eradication of pathogens and contributes to the development of biologically active multifunctional nanomaterials by rational design.

KEYWORDS: *$Mo_xRe_{1-x}S_2$ nanosheets, TMDC, 2D nanosheets, photothermal, nanozyme, antifungal, C. albicans infection*

■ INTRODUCTION

Fungal diseases cause over 1.5 million deaths and affect more than a billion people worldwide, presenting a major global public health challenge.[1,2] Currently, the persistent use and escalating dosages of antibiotics have resulted in rapid multidrug resistance and a decrease in treatment effectiveness.[3,4] *Candida albicans* (*C. albicans*) is a naturally occurring fungus in humans, typically found in small amounts in the mouth, on the skin, and in the intestines.[4,5] Its overproduction leads to a wide spectrum of infections, which renders it one of the most prevalent fungal pathogens in humans. Recently, the World Health Organization (WHO) has classified fungi like the *Candida* species as a top-priority microbial threat to global health, highlighting the urgent need for effective treatment approaches.[6]

Nanomaterials have attracted growing interest for their potential use as antifungal agents.[7] Among these, transition metal dichalcogenides (TMDCs), characterized by the general formula MX_2 (where M is a transition metal and X is a chalcogen element) exhibit diverse properties such as large surface area and semiconducting properties including tunable band gaps. Recently, TMDCs were explored in biomedical applications showing promise as alternatives to traditional antibiotics.[8,9] For example, MoS_2 was reported to possess peroxidase-like catalytic properties while exhibiting good biocompatibility, suggesting its usefulness in photothermal therapy (PTT) of cancer.[10] Owing to their distinctive

Received: October 21, 2024
Revised: November 1, 2024
Accepted: November 1, 2024
Published: November 14, 2024

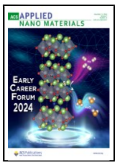

https://doi.org/10.1021/acsanm.4c05939
ACS Appl. Nano Mater. 2024, 7, 27717−27727

nanoarchitecture, the hybrid nanoparticle MSN-ReS_2 provides a bactericidal effect with photothermal therapy (PTT) in vitro.[11]

Peroxidases (also known as peroxide reductases) belong to a large group of enzymes that catalyze the oxidation of a substrate by hydrogen peroxide (H_2O_2).[12] The hydrogen peroxide is converted into water (H_2O) while oxidizing its substrate to the corresponding oxide form.[13,14] Nanozymes, nanomaterials with enzyme-like behavior in biological systems, present a promising alternative to traditional enzymes. Among various nanozymes, those mimicking peroxidase (POD) activity, known as POD nanozymes, are particularly of interest[14,15] due to their impressive broad-spectrum antimicrobial properties, low biological toxicity, low risk of inducing multidrug resistance, and unique mechanisms of sterilization.[14,16]

TMDCs (MoS_2, ReS_2, WS_2, etc.) exhibit POD-like activity as well as photothermal properties;[17−20] however, mixed sulfide nanozymes have not been explored to date in antifungal applications. According to literature reports, $Mo_xRe_{1-x}S_2$ with variable x display photoelectric properties.[21] Given our recent reports on photothermal effects of ReS_2 as a bactericide, we aimed to explore the synergy of POD-like characteristics of MoS_2 and photothermal capabilities of ReS_2, utilizing mixed-metal 2D $Mo_xRe_{1-x}S_2$ as a nanozyme/photothermal reagent showing the dual capacity in possible fungicide applications. In this work, we demonstrated the synthesis of compositionally tuned mixed-metal $Mo_xRe_{1-x}S_2$ nanozymes via hydrothermal synthesis and explored their application as POD-like antifungal reagents.

The materials' crystal structures have been validated by X-ray diffraction (XRD), and their morphology has been validated by scanning electron microscopy (SEM) and transmission electron microscopy (TEM). Elemental mapping analysis was conducted via SEM electron dispersive X-ray spectroscopy (EDS) and X-ray fluorescence spectroscopy (XRF). Both techniques confirmed that the Mo, Re, and S elements are uniformly distributed, indicative of homogeneous composition. The antifungal efficacy using the spread plate method, fluorescence probe staining, and SEM confirmed that $Mo_xRe_{1-x}S_2$ nanospheres (NSs) possess significant antifungal properties, enhanced with NIR irradiation.

■ EXPERIMENTAL SECTION

Materials. Hydrochloric acid (HCl, 37%), ammonium perrhenate (VII) (NH_4ReO_4, >99%), thiourea (99%), hydroxylamine hydrochloride ($NH_2OH\cdot HCl$, >99%), sodium hydroxide (NaOH), glutaraldehyde (50%), ammonium orthomolybdate(VII) ($(NH_4)_2MoO_4$, >99%), and ethanol (200 proof, 100% by volume) were purchased from ThermoFisher Scientific (Waltham, MA). Propidium iodide (PI) was provided by Biotium (Fremont, CA). Sabouraud dextrose broth (SDB) and Sabouraud dextrose agar (SDA) were purchased from Research Products International (Mount Prospect, IL). Dulbecco's phosphate-buffered saline (PBS, pH 7.4) without magnesium and calcium was purchased from Biosynth Lonza Bioscience (Walkersville, MD). Stabilized 3,3′,5,5′-tetramethylbenzidine (TMB) and H_2O_2 stock solutions and the IL-6 ELISA test kit were provided by R&D Systems Inc. (Minneapolis, MN). Cell Counting kit-8 (CCK-8) was purchased from GLPBIO Technology Inc. (Montclair, CA). Acridine orange (AO), and Gibco Dulbecco's Modified Eagle Medium (DMEM) were also purchased from ThermoFisher Scientific (Waltham, MA). *C. albicans* ATCC 10231 was purchased from Fisher Scientific.

Characterization. Scanning electron microscopy (SEM) imaging was conducted using a JEOL/JSM-F100 Schottky field emission scanning electron microscope (FE-SEM). X-ray fluorescence (XRF) measurements were carried out using a micro-XRF spectrometer (ATLAS M, IXRF Systems, Inc. Austin, Texas, USA). Ultraviolet−visible absorption spectroscopy was performed with a Thermo Scientific/BioMate 160 UV−visible spectrophotometer. Zeta potential and particle size analyses were carried out at room temperature using a Malvern/Zetasizer Nano-ZSZEN3600. X-ray diffraction (XRD) measurements were conducted using a Rigaku MiniFlex600 equipped with Cu Kα radiation (λ = 1.5405 Å) operating at 40 mV and 30 mA. Raman spectroscopy was carried out using a WITec alpha300 R confocal Raman microscope equipped with a 532 nm laser. pH measurements were performed with a FE 150 pH meter. An EVOS M7000 System (Thermo Fisher) was used for confocal microscopy imaging. Thermal images were collected with a thermal imaging camera (Teledyne FLIR).

Synthesis of $Mo_xRe_{1-x}S_2$ Nanozymes. Five different compositions of the $Mo_xRe_{1-x}S_2$ materials were prepared via a hydrothermal synthesis with the following intended different compositions: MoS_2, $Mo_{0.25}Re_{0.75}S_2$, $Mo_{0.5}Re_{0.5}S_2$, $Mo_{0.75}Re_{0.25}S_2$, and ReS_2.

In a typical experiment, predetermined amounts of ammonium orthomolybdate(VII) ($(NH_4)_2MoO_4$) and ammonium perrhenate(VII) (NH_4ReO_4) were dissolved in 60 mL of deionized water under stirring, totaling 1.2 mmol of Mo and Re metal precursors as per Table S1 (Supporting Information), at selected ratios of 0:4, 1:3, 2:2, 3:1, 4:0. Hydroxylamine hydrochloride (125.08 mg, 1.8 mmol) and thiourea (205.54 mg, 2.7 mmol) were then added to the mixture, and the mixture was stirred for 1 h. For each composition, the resulting solution was then transferred to an autoclave which was tightly sealed, introduced into a box furnace, and allowed to react for 24 h in a furnace at 230 °C. After the reaction, the autoclave was cooled to room temperature, and the product was collected by centrifugation (8000 rpm for 15 min). To remove any unreacted precursors, the product was washed three times with deionized water. The resulting $Mo_xRe_{1-x}S_2$ was collected by centrifugation and dried in a vacuum oven.

Photothermal Properties of $Mo_xRe_{1-x}S_2$ Nanozymes. The suspensions of $Mo_xRe_{1-x}S_2$ at a 200 μg/mL concentration were prepared by sonication in nanopure water. The experiments were performed in 96 well plates; 200 μL of solution was added to each well. Each sample (well) was irradiated for 10 min with an 808 nm near-infrared laser (Roithner Lasertechnik GmbH/RLDH808-1200-5) at a power density of 1 W/cm^2. The temperature of the solution was recorded at 10 s intervals using a digital thermometer (Physitemp/TH-5) connected to a microprobe thermocouple. After 10 min of irradiation, the laser was turned off, and the temperature drop was measured in the same manner. The process was repeated for five cycles of heating and cooling to test the photothermal stability. Additionally, $Mo_xRe_{1-x}S_2$ suspensions at different concentrations (0, 50, 100, 200 μg/mL) were prepared in 200 μL volume in nanopure water, placed in 1.5 mL Eppendorf tubes (EP tubes), and treated in the same manner. Thermal images were captured at an interval of 2 min with a thermal camera. The photothermal conversion efficiency (η) was calculated based on previously reported methods.[11]

Cell Viability Assay for Biocompatibility Testing. The HeLa cell line was purchased from Antibody Research Corporation (Saint Charles, MO, USA). The cells were cultured in DMEM, supplemented with 10% heat-inactivated fetal bovine serum, 0.1 g/L streptomycin sulfate, and 0.1 g/L penicillin G. They were incubated at 37 °C in a humidified atmosphere of 5% CO_2. The cell viability assay was performed using a Cell Counting Kit-8 (CCK-8 kit). CCK-8 utilizes a tetrazolium salt, WST-8, which is converted to the water-soluble WST-8 formazan. The amount of formazan produced is proportional to the number of viable cells and can be quantified by measuring the absorbance at 450 nm.[22] Initially, HeLa cells were seeded into 96-well plates (Corning Costar, Corning, NY) at a density of 1.0×10^3 cells per well in 100 μL of medium to evaluate the biocompatibility of $Mo_xRe_{1-x}S_2$. After incubation for 24 h, cell viability was assessed using a CCK-8 assay with various concentrations of $Mo_xRe_{1-x}S_2$ (0−200 μg/mL). Subsequently, 10 μL of

Scheme 1. Oxidation of TMB Using H_2O_2

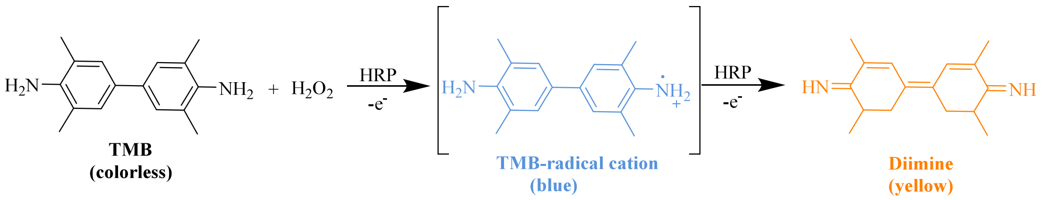

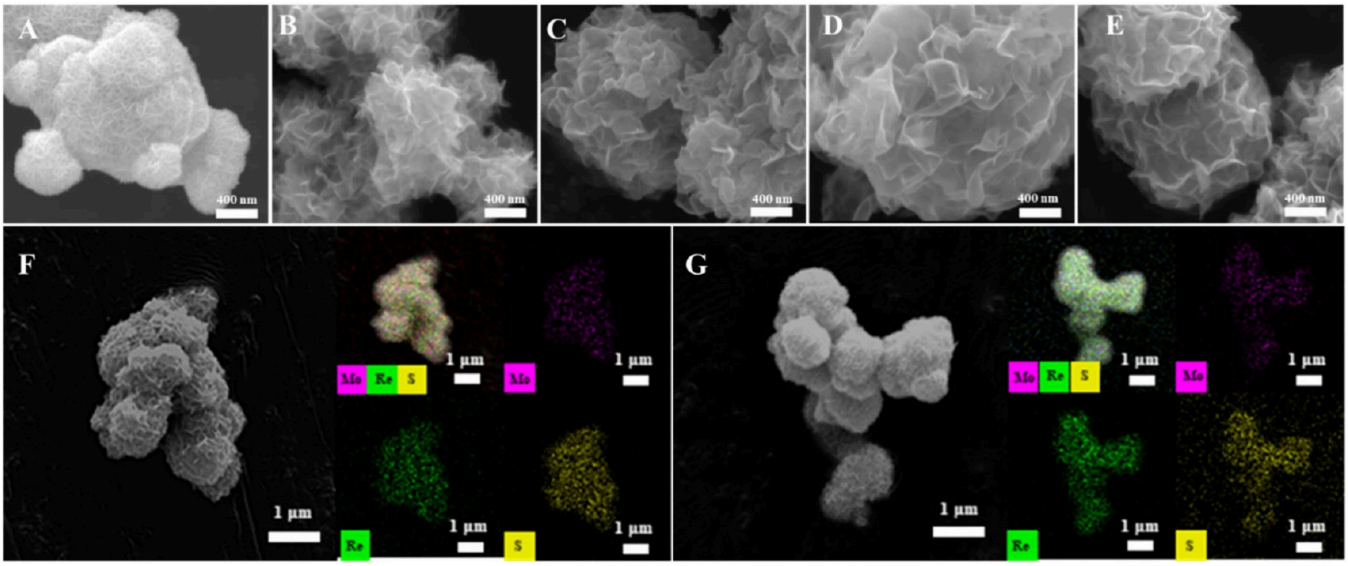

Figure 1. SEM images of $Mo_xRe_{1-x}S_2$ NSs (A: ReS_2, and B: $Mo_{0.42}Re_{0.58}S_{1.94}$, C: $Mo_{0.66}Re_{0.34}S_{1.85}$, D: $Mo_{0.81}Re_{0.19}S_{1.76}$, and E: MoS_2) and elemental mapping analysis (F: $Mo_{0.66}Re_{0.34}S_{1.85}$, and G: $Mo_{0.81}Re_{0.19}S_{1.76}$).

CCK-8 solution was added to each well, and the plates were incubated for an additional 2 h before absorbance measurement.

Culture and Preparation of *C. albicans*. In this work, all of the tests of antifungal activity were evaluated against *C. albicans*. Both Sabouraud dextrose broth (SDB) and Sabouraud dextrose agar (SDA) media used in this study were sterilized in an autoclave at 121 °C for 25 min. The strain of *C. albicans* was stored in SDB supplemented with 20% glycerol at −80 °C. The glycerol stock containing the strain was thawed and revived on an SDA plate at 37 °C for 24 h. Next, a single colony was transferred using a sterile inoculation loop into a 15 mL sterile polypropylene round-bottom culture tube containing 5 mL of SDB and incubated in a shaking incubator at 37 °C and 180 rpm. After 12 h of incubation, the strains were centrifuged at 1000 rpm for 5 min and washed once with PBS, and the fungi were ready for immediate use.

POD-like Activity of the Nanozymes. To quantify the catalytic efficiency and specificity of $Mo_xRe_{1-x}S_2$ toward the POD substrate, Michaelis−Menten kinetics of the catalytic process were further investigated. In this work, the POD-like activity of the nanozymes was studied by varying the concentration of TMB or H_2O_2 while keeping the other conditions constant. Stock solutions of TMB and H_2O_2 were prepared at 1.66 M (0.4 g/L) and 0.2 M, respectively. As illustrated in Scheme 1, oxidation of TMB by a model peroxidase, horse radish peroxidase (HRP), in the presence of H_2O_2 leads first to the blue-colored TMB radical cation, followed by its further oxidation to the yellow-colored diimine. Lineweaver−Burk plots were generated to determine the Michaelis−Menten constant (K_m) for TMB and H_2O_2, respectively. A lower K_m value indicates a higher affinity between the enzyme and the substrate.[23]

Antifungal Activity. The antifungal activity testing was conducted in 96-well plates as described above. An amount of 50 µL of fungal suspension (1×10^8 colony-forming units (CFU) per mL) was added to each well, followed by the addition of 50 µL of H_2O_2 solution (3 mM). A stock solution of nanozyme was prepared at 1 mg/mL, and different amounts of $Mo_xRe_{1-x}S_2$ were dispensed into each well to reach the desired concentrations (7.5 µL for 0.025 mg/mL; 15 µL for 0.05 mg/mL, and 30 µL for 0.1 mg/mL), using PBS to adjust the final total volume to 300 µL. The antifungal activity was evaluated under the treatment of the nanozyme both alone and combined with laser irradiation at 808 nm. After the nanozyme exposure, the antifungal effect of $Mo_xRe_{1-x}S_2$ was evaluated using the spread plate method.[24] An amount of 10 µL of fungal suspension from each 96-well plate was evenly spread on the surface of agar plates, and after that, the plates were placed in the 37 °C incubator for 24 h. The number of fungal colony-forming units was counted and compared to the control group. The experiments were conducted in a biosafety cabinet and repeated thrice. The fungi survival rate was calculated using eq 1.

$$\text{Viability}\ (\%) = \frac{\#\ \text{of colonies formed in the ep group}}{\#\ \text{of colonies formed in the control group}} \times 100 \tag{1}$$

***C. albicans* Staining Test.** Acridine orange (AO)/propidium iodide (PI) staining was used for the live and dead *C. albicans* staining.[11] The protocol of the live/dead bacteria staining test with the AO/PI staining solution is described in the Supporting Information (SI). The concentration of the fungal stock suspension in the staining test was 1.0×10^8 CFU·mL^{-1}. After treatment, 100 µL of a *C. albicans* suspension was centrifuged and resuspended in 0.85% NaCl. Then, the samples were stained with the prepared AO/PI solution at 37 °C in the dark for 1 h. Next, 5 µL of the stained mixture was placed onto a microscope cover glass (18 mm × 18 mm), and then placed upside down on a microscope slide and sealed on all sides. A confocal fluorescence microscope was employed to capture images, with the green fluorescence signal at 488 nm indicating live cells and the red fluorescence signal at 561 nm indicating dead cells.[11]

Imaging of *C. albicans* Morphology. For SEM imaging, each *C. albicans* specimen was prepared by the following method.[25] The

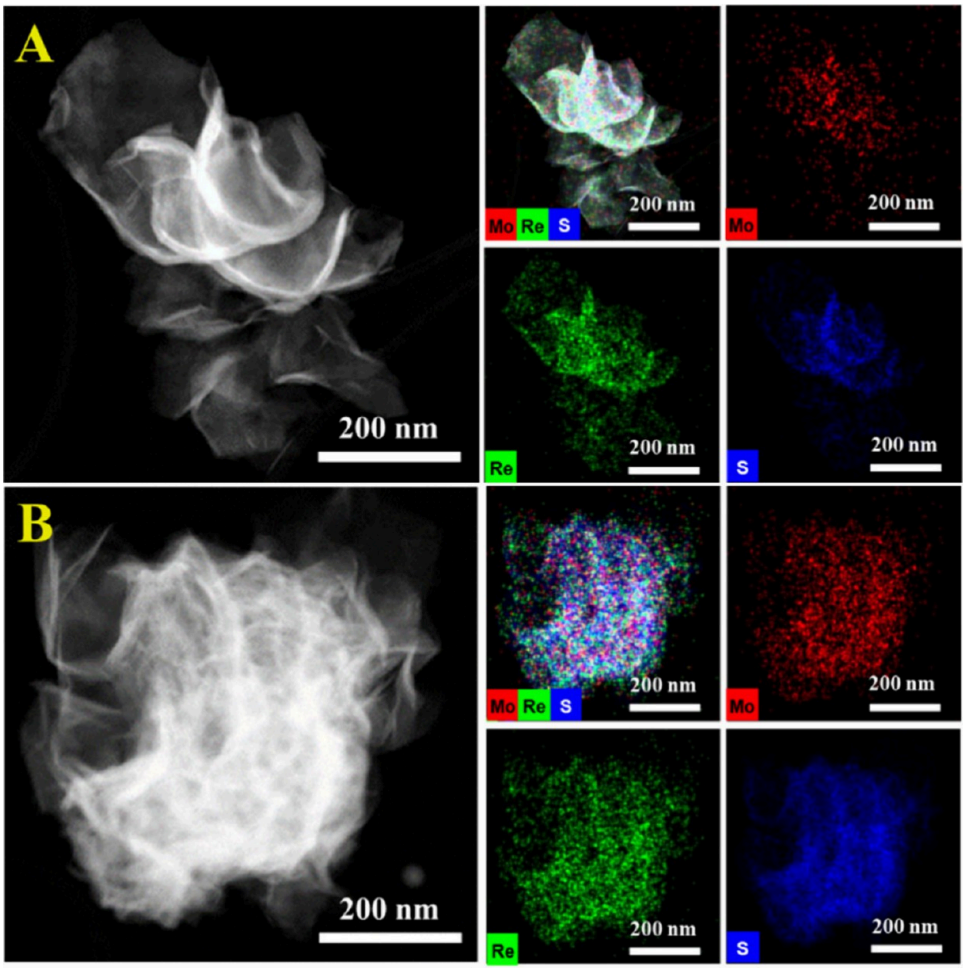

Figure 2. TEM and elemental mapping analysis of $Mo_{0.66}Re_{0.34}S_{1.85}$ (A) and $Mo_{0.81}Re_{0.19}S_{1.76}$ (B).

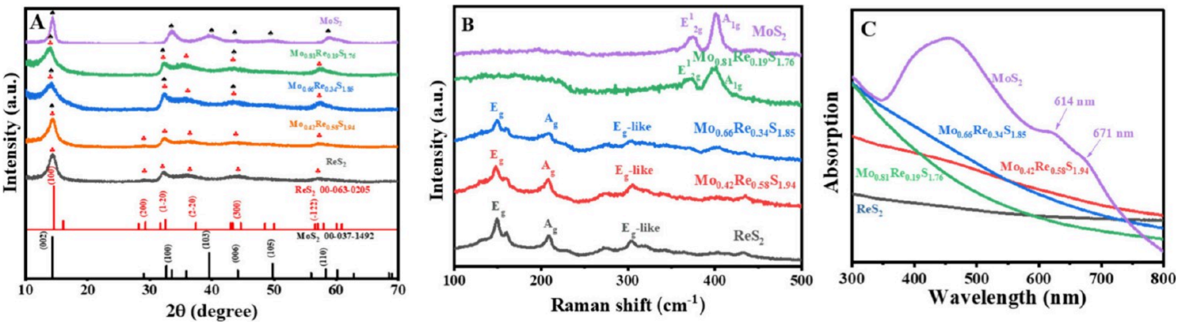

Figure 3. XRD pattern (A), Raman spectra (B), and absorption spectrum (C) of prepared $Mo_xRe_{1-x}S_2$ NSs.

experiment was conducted in a 96-well plate. A fungal stock suspension was prepared at 1.0×10^8 CFU·mL^{-1}. An amount of 100 μL of fungal suspension was added to each well, followed by the addition of 50 μL of H_2O_2 solution (3 mM), 30 μL of $Mo_xRe_{1-x}S_2$ solution (1 mg/mL), and 120 μL of PBS to adjust the final total volume to 300 μL. Next, the samples were subjected to irradiation at 808 nm. The group without $Mo_xRe_{1-x}S_2$ was a control to observe the morphology of the fungi. After treatment, the 96-well plate was placed in an incubator for 1 h. Next, the solutions from each well were transferred to 1.5 mL microcentrifuge tubes and centrifuged once (4000 rpm, 3 min) to remove the supernatant and redispersed into 200 μL of glutaraldehyde (2.5% in PBS) for fixation. After fixation for 24 h, the samples were dehydrated through an ethanol series, by submerging in 500 μL of ethanol solutions of progressively increasing concentrations (10, 30, 50, 70, 90, and 100%), with each step lasting 10 min. Subsequently, each fungal suspension was mixed with 15 μL of ethanol, and a 5 μL drop of this mixture was placed onto a 9 mm circular cover glass. These cover glasses were then dried overnight in an oven. The dried circular cover glass samples were affixed to the sample holder using tape and sputter-coated with gold (Au) to achieve a coating approximately 5 nm thick. Each sample was imaged by SEM at 10.0 kV and SEM EDX at 3 kV.

Statistical Analysis. All data were organized into tables as mean ± standard deviation (SD). Comparisons among the experimental groups were performed using Student's multiple *t* test, with $p < 0.05$ (*), $p < 0.01$ (**), and $p < 0.001$ (***) considered statistically significant.

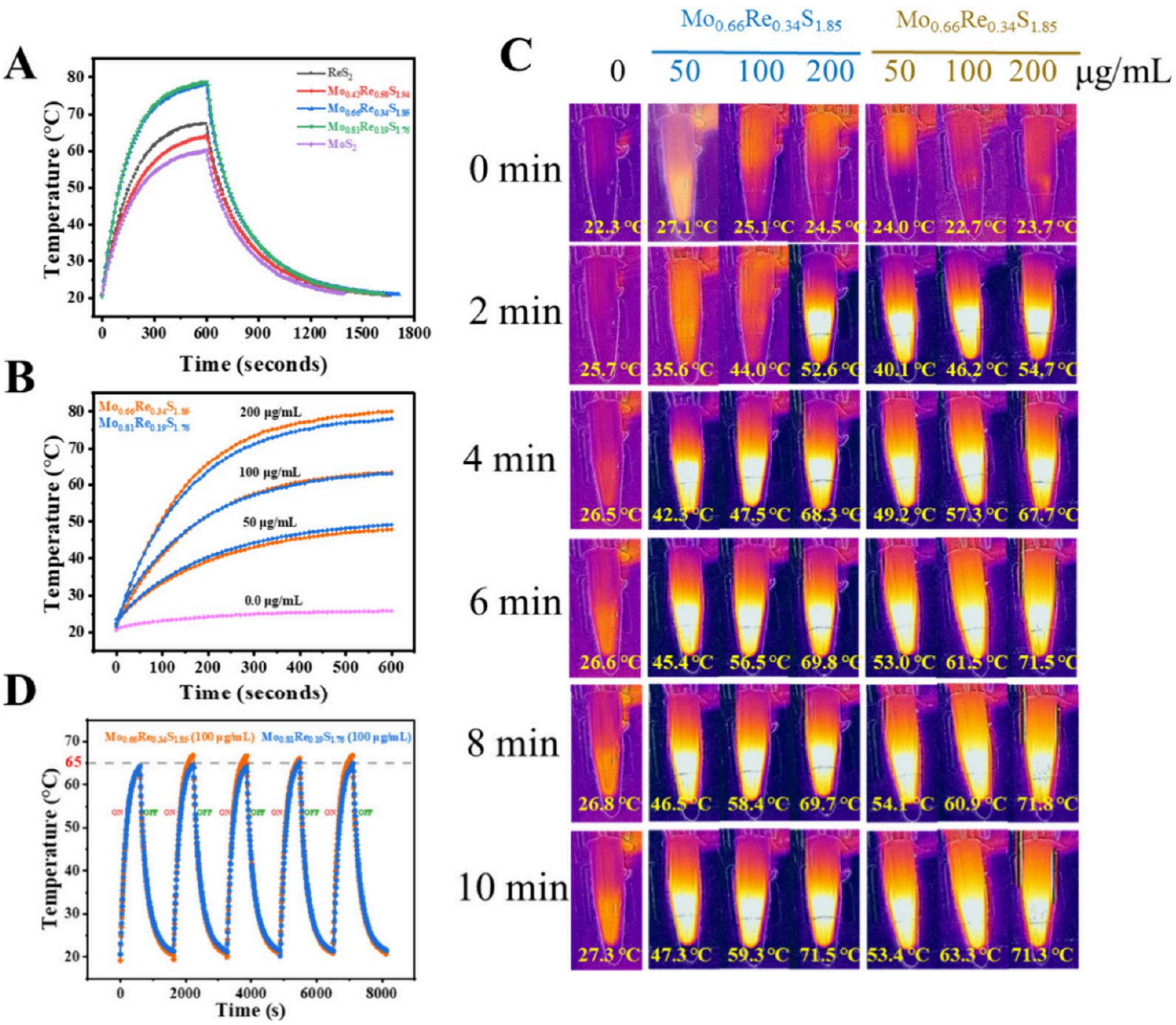

Figure 4. (A) Temperature profile of Mo$_x$Re$_{1-x}$S$_2$ nanozyme suspension (200 μg/mL) as a function of time, when irradiated with IR light waves (808 nm, 1 W/cm^2) followed by natural cooling without irradiation. (B) Temperature profiles (heating only) of Mo$_{0.66}$Re$_{0.34}$S$_{1.85}$ and Mo$_{0.81}$Re$_{0.19}$S$_{1.76}$ nanozymes ar different concentrations (0−200 μg/mL) and (C) corresponding thermal images captured of different periods 0−10 min. (D) Photothermal stability of Mo$_{0.66}$Re$_{0.34}$S$_{1.85}$ and Mo$_{0.81}$Re$_{0.19}$S$_{1.76}$ nanozyme suspension (100 μg/mL) for successive 5 cycles of irradiation.

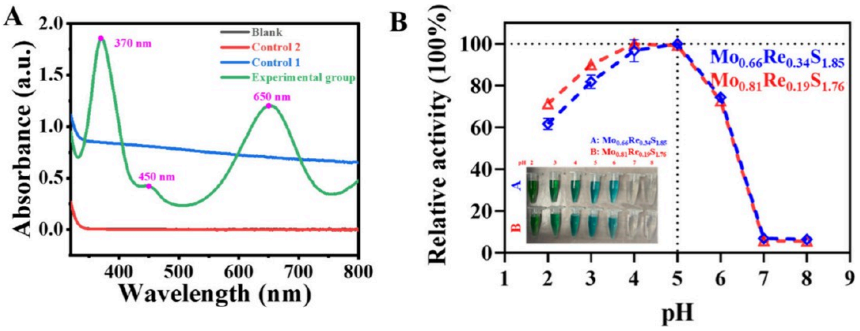

Figure 5. (A) Absorption spectra of different systems. Blank: TMB and H$_2$O$_2$ were mixed without a catalyst; control 1: TMB and catalyst were mixed without H$_2$O$_2$; control 2: H$_2$O$_2$ and catalyst were mixed without TMB; experimental group: TMB and H$_2$O$_2$ were mixed with a catalyst. (B) Effects of different pH values (2.2−8) on relative POD activity for Mo$_{0.66}$Re$_{0.34}$S$_{1.85}$ and Mo$_{0.81}$Re$_{0.19}$S$_{1.76}$ nanozymes.

■ RESULTS AND DISCUSSION

Nanomaterials Characterization. *Nanoparticle Morphology.* The surface morphology of the Mo$_x$Re$_{1-x}$S$_2$ NSs was observed by SEM (Figure 1A−E). The morphology of Mo$_x$Re$_{1-x}$S$_2$ is flower-like and consists of nanosheets self-assembled layer by layer. The SEM EDX analysis in Figure S1 revealed that the intended compositions Mo$_{0.25}$Re$_{0.75}$S$_2$, Mo$_{0.5}$Re$_{0.5}$S$_2$, and Mo$_{0.75}$Re$_{0.25}$S$_2$ resulted in products with elemental compositions of Mo$_{0.42}$Re$_{0.58}$S$_{1.94}$, Mo$_{0.66}$Re$_{0.34}$S$_{1.85}$, and Mo$_{0.81}$Re$_{0.19}$S$_{1.76}$, respectively. The SEM elemental mapping results also revealed that the molybdenum (Mo),

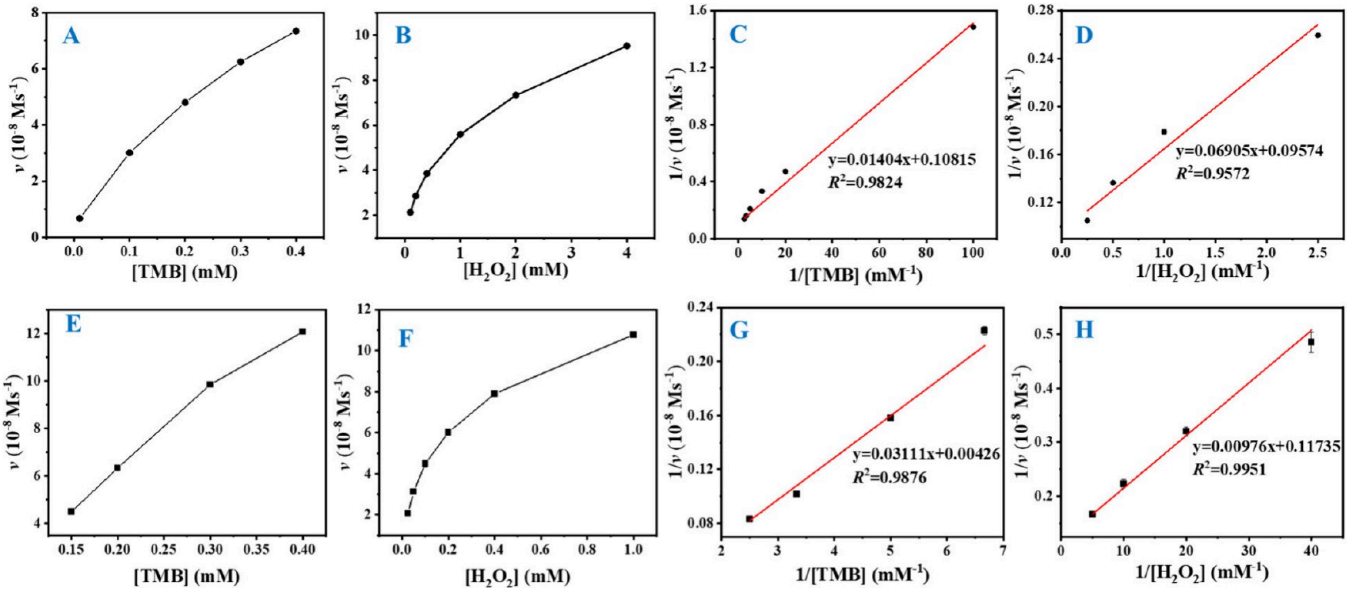

Figure 6. Steady-state kinetic assay of peroxidase-like activity of $Mo_{0.66}Re_{0.34}S_{1.85}$ and $Mo_{0.81}Re_{0.19}S_{1.76}$ (pH 5) at room temperature as a function of [TMB] in panels (A) and (E) and H_2O_2, in panels (B) and (F), and corresponding double-reciprocal plots (C) corresponding to (A); (G) to (E), (D) to (B), and (H) to (F). (A) The concentration of H_2O_2 was 2 mM and TMB was varied (0.01−0.4 mM). (B) TMB concentration was fixed at 1.66 mM and H_2O_2 was varied (0.1−4 mM). (E) The concentration of H_2O_2 was 2 mM and TMB was varied (0.01−0.4 mM). (F) TMB concentration was fixed at 1.66 mM and H_2O_2 was varied (0.1−1.0 mM).

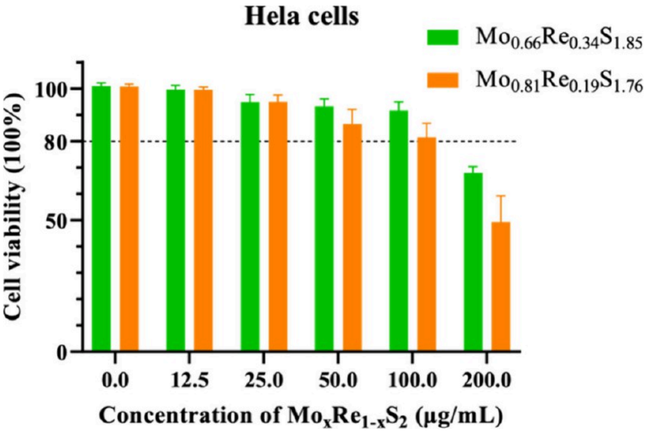

Figure 7. Cell viability experiments in the HeLa cell line after treatment with $Mo_{0.66}Re_{0.34}S_{1.85}$ and $Mo_{0.81}Re_{0.19}S_{1.76}$ nanoparticles at different concentrations (12.5, 25, 50, 100, and 200 mg/mL) for 24 h. HeLa cells treated with PBS were used as a control.

rhenium (Re), and sulfur (S) elements were uniformly distributed in two of the compositions, $Mo_{0.66}Re_{0.34}S_{1.85}$ and $Mo_{0.81}Re_{0.19}S_{1.76}$, as shown in Figure 1F,G, respectively.

To further elucidate the morphologies and compositions of the $Mo_xRe_{1-x}S_2$ NSs, high magnification TEM imaging and TEM/EDS elemental mapping of $Mo_{0.66}Re_{0.34}S_{1.85}$ and $Mo_{0.81}Re_{0.19}S_{1.76}$ were conducted (Figure 2A,B, respectively). The TEM imaging confirmed that $Mo_{0.66}Re_{0.34}S_{1.85}$ and $Mo_{0.81}Re_{0.19}S_{1.76}$ exhibit a flower-like morphology formed of self-assembled nanosheets. High-resolution elemental mapping of $Mo_{0.66}Re_{0.34}S_{1.85}$ and $Mo_{0.81}Re_{0.19}S_{1.76}$ further validated the uniform distribution of Mo, Re, and S elements.[26]

X-ray Fluorescence (XRF). XRF was employed to further confirm the homogeneity of elemental composition of $Mo_{0.66}Re_{0.34}S_{1.85}$ and $Mo_{0.81}Re_{0.19}S_{1.76}$. The elemental mapping analysis by X-ray fluorescence (Figure S2, SI) confirmed the different percentages of the alloyed metal sulfides.

X-ray Powder Diffraction. The as-synthesized nanopowders of $Mo_xRe_{1-x}S_2$ were characterized by XRD to analyze the crystallographic changes with increasing the Mo content, as presented in Figure 3A. The standard patterns of the pure ReS_2 (JCPDS No. 00-063-0205) and MoS_2 (JCPDS No. 00-037-1492) are also displayed in Figure 3A.

Pure MoS_2 and $ResS_2$ display X-ray diffraction patterns that are quite similar due to their very similar crystal structure. As a result the mixed-metal chalcogenides $Mo_xRe_{1-x}S_2$ (with $0 < x < 1$) show high similarity to the pure ones. Slight peak shifts could be attributed to the unit cell parameters expanding and the interplanar spacing increasing with increased Mo content.[27,28]

To explore the reaction mechanism underlying the formation of $Mo_xRe_{1-x}S_2$ and understand the correlation between final product composition and reaction time, different reaction times were explored for synthesizing $Mo_{0.66}Re_{0.34}S_{1.85}$. The products were analyzed by XRD (Figure S4), TEM (Figure S5), and XRF (Figure S6). The stability of the synthesized $Mo_xRe_{1-x}S_2$ nanoenzyme in acidic conditions, in the pH range of 2.2−5 was evaluated by exposing $Mo_{0.66}Re_{0.34}S_{1.85}$ and $Mo_{0.81}Re_{0.19}S_{1.76}$ to solutions with different pH (2.2−5.0) for 16 h; the solution preparation is shown in Table S2. XRD patterns of materials collected after exposure are shown in Figure S7. Notably, no discernible changes were observed in the XRD spectrum across the different pH conditions, indicating that the crystalline structures of both samples were unaffected by the acidic treatment, indicative of crystal lattice stability under the mildly acidic environment.

Raman Spectroscopy. Raman spectra were collected to confirm the phase structure of the nanozymes. Figure 3B presents the Raman spectra of $Mo_xRe_{1-x}S_2$ with increasing Mo content. $Mo_xRe_{1-x}S_2$ nanostructures exhibit main vibration modes in the range of 100−500 cm^{-1} corresponding to the E_g-

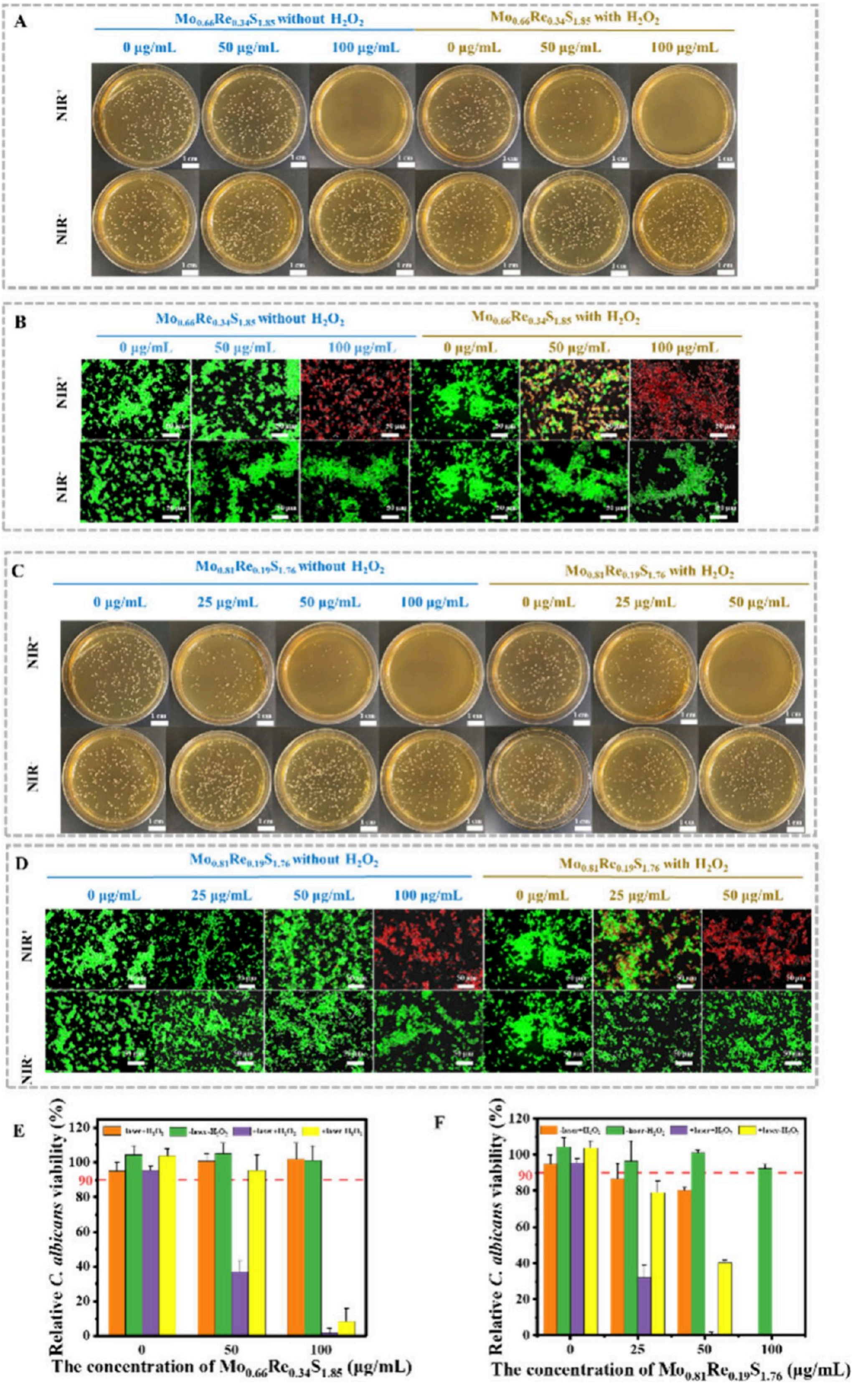

Figure 8. (A, C) Photographs of the SDA agar plates with *C. albicans* following different treatments with varying concentrations of $Mo_{0.66}Re_{0.34}S_{1.85}$ and $Mo_{0.81}Re_{0.19}S_{1.76}$ and (B, D) corresponding fluorescence staining confocal images of *C. albicans* using AO/PI taken after 1 h of different treatments. (E, F) Relative viability of *C. albicans* after various treatments were applied to the agar plates.

like, A_g-like modes of ReS_2. Specifically, vibrational modes centered at 150.4 and 208.3 cm^{-1} correspond to the in-plane (E_g) and primarily out-of-plane (A_g-like) modes of ReS_2. As Mo content increased ($x > 0.65$) two characteristic bands

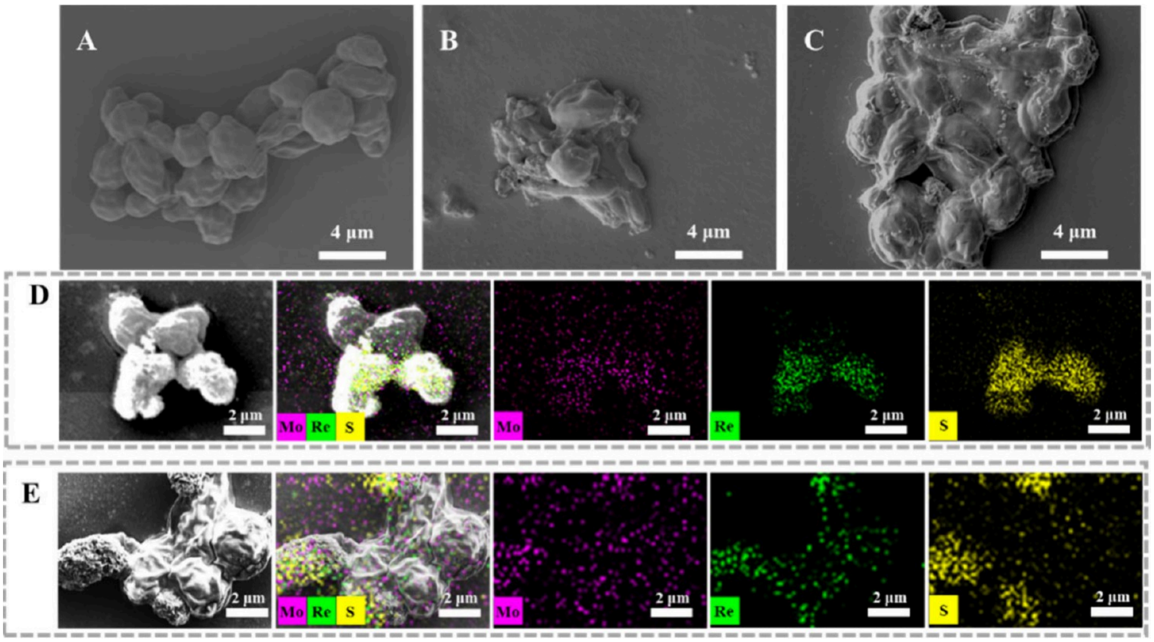

Figure 9. SEM images of the fungi under different treatments (A: blank control, B: treated with $Mo_{0.66}Re_{0.34}S_{1.85}$, C: treated with $Mo_{0.81}Re_{0.19}S_{1.76}$). SEM elemental mapping analysis of the fungi under different treatments (D: treated with $Mo_{0.66}Re_{0.34}S_{1.85}$, E: treated with $Mo_{0.81}Re_{0.19}S_{1.76}$).

located at 374.4 and 402.2 cm^{-1}, which are attributed to the E_{2g} and A_{1g} modes of MoS_2, appeared. The E_{2g} band is due to in-plane vibrations, and the A_{1g} band is due to out-of-plane vibrations.[29,30] Additionally, E_g and second-order vibrational modes appear due to the low crystal symmetry.[31] The differences in the magnitude of the shifts observed for both bands provide insight into the doping mechanism.[32] Compared to the Raman spectrum of MoS_2, the A_{1g} mode, which involved only the vibrational displacement of sulfur atoms, showed a slight shift from ca. 402.2 cm^{-1} to ca. 397.8 cm^{-1} in $Mo_{0.81}Re_{0.19}S_{1.76}$. In contrast, the E^1_{2g} mode, which involves the vibration of both metal and sulfur atoms within a layer, exhibits a significant shift from ca. 374.4 cm^{-1} to 369.9 cm^{-1}. This could be ascribed to the substitutional doping of the heavier Re atoms into the Mo layer.[23] As the Re ratio increases in $Mo_xRe_{1-x}S_2$, the peaks of E_g, A_g, and E_g-like become sharper and more defined, like those of ReS_2.

The absorption spectrum in Figure 3C shows the variation in absorbance with increasing Mo content in $Mo_xRe_{1-x}S_2$. As shown in Figure 3C, only MoS_2 exhibited an absorption peak at 671 nm corresponding to the direct band gap of 1.85 eV. The absorption intensity sharply decreased compared to that of MoS_2 as the Re-doping concentration increased. This is due to the new gap states with Re doping, also causing band gap narrowing.[26] The band gap narrowing causes a shift in absorption in the NIR region, and therefore, it could impact photothermal performance. To confirm this hypothesis, different compositions of $Mo_xRe_{1-x}S_2$ were subjected to photothermal experiments.

Particle Size and Charge. The particle size distribution and zeta potential were determined by using dynamic light scattering (DLS). As shown in Figure S3A, the particle size of $Mo_{0.66}Re_{0.34}S_{1.85}$ and $Mo_{0.81}Re_{0.19}S_{1.76}$ is in the range of 80–300 nm with average particle size of about 162 and 119 nm, respectively. As reported, cationic nanoparticles penetrate cellular membranes, destabilizing the entire membrane structure enough to destroy the cell at higher concentrations.[33] Given the negative charge of $Mo_{0.66}Re_{0.34}S_{1.85}$ and $Mo_{0.81}Re_{0.19}S_{1.76}$, they would not interfere with healthy human cells and disrupt their membranes in practical antifungal applications, exploiting only the catalytic pathway to effectively kill fungi.

Photothermal Performance of $Mo_xRe_{1-x}S_2$. Samples of each nanozyme (200 μg/mL dispersed in H_2O) were exposed to near-infrared laser light (808 nm) of intensity 1 W/cm^2 for 10 min, and the temperature variation was measured at intervals of 10 s. After 10 min, the laser was turned off, and the temperature was measured continuously until it reached room temperature. Figure 4A shows the temperature profiles of all $Mo_xRe_{1-x}S_2$ nanozyme samples as a function of time. The samples with compositions $Mo_{0.66}Re_{0.34}S_{1.85}$ and $Mo_{0.81}Re_{0.19}S_{1.76}$ achieved the highest temperature of 80 °C (after 600 s) compared to the other samples. The photothermal conversion efficiency (η) of $Mo_xRe_{1-x}S_2$ was calculated using eq 2.[11]

$$\eta = \frac{hA(\Delta T_{\mathrm{max,mix}} - \Delta T_{\mathrm{max,H_2O}})}{I(1 - 10^{-A_{808}})} \quad (2)$$

where A is the surface area of the container, h is the heat transfer coefficient, $\Delta T_{\mathrm{max,mix}}$ and $\Delta T_{\mathrm{max,H_2O}}$ are the temperature changes of the $Mo_xRe_{1-x}S_2$ and solvent (water), respectively, at the maximum steady-state temperature, I represents the laser power, and A_λ is the absorbance of $Mo_xRe_{1-x}S_2$ NSs at 808 nm.

The calculated values of η for $Mo_xRe_{1-x}S_2$ nanozymes are presented in Table S3. The nanozymes with a composition of $Mo_{0.66}Re_{0.34}S_{1.85}$ and $Mo_{0.81}Re_{0.19}S_{1.76}$ exhibit η = 21.6% and 21.8%, respectively, which were higher compared to that of ReS_2 (17.2%), $Mo_{0.42}Re_{0.58}S_{1.94}$ (16.4%), and MoS_2 (16.1%).

The $Mo_{0.66}Re_{0.34}S_{1.85}$ and $Mo_{0.81}Re_{0.19}S_{1.76}$ nanozymes were further explored for photothermal studies. To identify the appropriate temperature for the in vitro assay, different concentrations (0–200 μg/mL) of the $Mo_{0.66}Re_{0.34}S_{1.85}$ and $Mo_{0.81}Re_{0.19}S_{1.76}$ nanozymes were tested (Figure 4B). Thermal images were collected, and the temperature change could be observed vividly in Figure 4C. H_2O served as the negative control and exhibited no significant temperature changes over 10 min (from 22.3 to 27.3 °C). However, with increasing concentration, the temperature gradually increased for 10 min. The materials showed high photothermal stability featured during five heating/cooling cycles under the same treatment, which provided consistent performance and potential for antifungal activity (Figure 4D).

POD-like Activity and Kinetic Study of $Mo_xRe_{1-x}S_2$. The POD-like activity of $Mo_{0.66}Re_{0.34}S_{1.85}$ and $Mo_{0.81}Re_{0.19}S_{1.76}$ nanozymes was evaluated by using a typical POD catalytic system with TMB and H_2O_2 as the substrates. Absorption spectra were recorded under the different experimental conditions. No characteristic peaks were observed when using TMB alone (control 1) or H_2O_2 alone (control 2) or when TMB and H_2O_2 were mixed without a catalyst (blank). Figure 5A indicates that TMB cannot be oxidized by H_2O_2 without a catalyst. However, with the addition of $Mo_xRe_{1-x}S_2$ nanozymes, strong absorption peaks appeared at 370 and 650 nm (experimental group), demonstrating the formation of oxidized TMB (oxTMB). In addition, the effect of pH on the catalytic activity was tested (Figure 5B), showing that from pH 2.2 to 5, relative POD activity exhibited a gradual increase, beginning at 60% and reaching its maximum activity at pH 5 (100%). However, as the pH increased from 5 to 6, the activity gradually decreased. The most significant decline in activity occurred between pH 6 and pH 7, where it dropped abruptly to nearly zero. Beyond pH 7, specifically at pH 8, no further change in activity was observed, indicating a complete loss of functional activity.

To quantify the catalytic efficiency and specificity of $Mo_xRe_{1-x}S_2$ toward the POD substrate, the Michaelis−Menten kinetics were further investigated. Experiments were conducted by varying the concentration of TMB or H_2O_2 while keeping the other conditions constant. Lineweaver−Burk plots were generated to determine the Michaelis−Menten constant (K_m) for TMB and H_2O_2 (Figure 6). A lower K_m value indicates a higher affinity between the enzyme and the substrate. Table S4 summarizes the linear fit data, and Table S5 provides the corresponding kinetic parameters. The K_m value for the $Mo_{0.81}Re_{0.19}S_{1.76}$ nanozyme with TMB as the substrate was 56 times higher than that of $Mo_{0.66}Re_{0.34}S_{1.85}$, whereas the V_{max} value of the $Mo_{0.81}Re_{0.19}S_{1.76}$ nanozyme was 25 times higher than that of $Mo_{0.66}Re_{0.34}S_{1.85}$. Conversely, the K_m value for the $Mo_{0.81}Re_{0.19}S_{1.76}$ nanozyme with H_2O_2 as the substrate was 9 times lower than that of $Mo_{0.66}Re_{0.34}S_{1.85}$, and its V_{max} value was 1.2 times lower. These results indicate that $Mo_{0.66}Re_{0.34}S_{1.85}$ has a higher affinity for TMB, while $Mo_{0.81}Re_{0.19}S_{1.76}$ has a higher affinity for H_2O_2, implying that the $Mo_{0.81}Re_{0.19}S_{1.76}$ nanozyme has a greater peroxidase-like activity.

Cell Viability Assay. To understand the antifungal potential of nanozymes in biomedical applications, it is critical to assess the biocompatibility of $Mo_xRe_{1-x}S_2$ before conducting further in vivo studies. The biocompatibility assay was performed using HeLa cells, incubated with $Mo_xRe_{1-x}S_2$ at various concentrations for 24 h; the cytotoxicity was evaluated using a CCK-8 assay. The results showed that low concentrations of $Mo_{0.66}Re_{0.34}S_{1.85}$ and $Mo_{0.81}Re_{0.19}S_{1.76}$ did not impact HeLa cell survival rates. However, at 100 μg/mL, the cell viability decreased to 90% and 80%, respectively (Figure 7). At concentrations of up to 200 μg/mL, $Mo_{0.66}Re_{0.34}S_{1.85}$ and $Mo_{0.81}Re_{0.19}S_{1.76}$ nanozymes exhibited toxicity in vitro. These results suggest that $Mo_xRe_{1-x}S_2$ has good biocompatibility at concentrations of up to 100 μg/mL.

Antifungal Activity and *C. albicans* Staining Test. Samples were examined for their antifungal activity against *C. albicans* by plating. Initially, *C. albicans* was treated with the same amount of H_2O_2 but different concentrations of $Mo_xRe_{1-x}S_2$ nanozymes at 808 nm laser for 10 min. As shown in Figure 8(A), the H_2O_2 control showed no killing compared with the PBS control, which means that the H_2O_2 itself is not toxic enough to kill the fungi in the test. With a concentration of 50 μg/mL $Mo_{0.66}Re_{0.34}S_{1.85}$, its POD-like activity showed noticeable fungi-killing, and 100 μg/mL $Mo_{0.66}Re_{0.34}S_{1.85}$ without H_2O_2 killed the fungi during the photothermal exposure. The $Mo_{0.81}Re_{0.19}S_{1.76}$ sample (Figure 6B) showed better peroxidase-like activity and antifungal effect in the presence of H_2O_2 than that of $Mo_{0.66}Re_{0.34}S_{1.85}$, using a lower concentration of nanozyme. The experiment was conducted in triplicate. Additionally, the antifungal effect of $Mo_{0.66}Re_{0.34}S_{1.85}$ and $Mo_{0.81}Re_{0.19}S_{1.76}$ nanozymes was directly observed through live/dead staining (AO and PI) of *C. albicans* after various treatments, aligning with the spread plate data. Figure 8B shows strong green fluorescence in three NIR^+ groups, including 0 μg/mL $Mo_{0.66}Re_{0.34}S_{1.85}$ with no H_2O_2 (group 1), 50 μg/mL $Mo_{0.66}Re_{0.34}S_{1.85}$ with no H_2O_2 (group 2), 0 μg/mL $Mo_{0.66}Re_{0.34}S_{1.85}$ with H_2O_2 (group 3) and all the NIR^- groups indicated that living colonies that could only take up AO. Conversely, strong red fluorescence was observed (Figure 8B) in the 100 μg/mL $Mo_{0.66}Re_{0.34}S_{1.85}$ and 100 μg/mL $Mo_{0.66}Re_{0.34}S_{1.85}$ with H_2O_2 NIR^+ groups represent dead *C. albicans* colonies capable of uploading PI. The yellow areas in the confocal images, a combination of the green and red fluorescence, suggest that some fungal membranes may have thinned or been damaged, allowing the PI dye to penetrate and bind to the DNA, staining the nucleus red. Figure 8C presents photographs of the SDA agar plates with *C. albicans* following different treatments of $Mo_{0.81}Re_{0.19}S_{1.76}$. Fluorescence confocal images in Figure 8D show yellow areas from the 25 μg/mL $Mo_{0.81}Re_{0.19}S_{1.76}$ + H_2O_2 NIR^+ group, while the 50 μg/mL $Mo_{0.81}Re_{0.19}S_{1.76}$ + H_2O_2 NIR^+ group exhibited only strong red fluorescence. These findings suggest a positive correlation between the peroxidase-like activity and the photothermal effect of $Mo_{0.66}Re_{0.34}S_{1.85}$ and $Mo_{0.81}Re_{0.19}S_{1.76}$ nanozymes and their antifungal activities.

The antifungal activities of $Mo_{0.66}Re_{0.34}S_{1.85}$ and $Mo_{0.81}Re_{0.19}S_{1.76}$ were also evaluated for the acidic pH treated samples (Figure S8, SI). The results suggest that the material activity is not impacted by an acidic environment and longer exposure does not diminish antifungal activity.

Imaging of *C. albicans* Morphology. To uncover the effects of interaction between $Mo_xRe_{1-x}S_2$ NSs and *C. albicans*, the morphological changes in *C. albicans* were examined by using SEM and SEM EDX. Figure 9 illustrates that the antifungal effects observed in the $Mo_{0.66}Re_{0.34}S_{1.85}$ and $Mo_{0.81}Re_{0.19}S_{1.76}$ groups were due to the surface collapse of *C. albicans*. The fungal skeletal structure was either significantly deformed or completely collapsed after the treatment. These findings confirmed that the photothermal effect and POD-like activity of $Mo_xRe_{1-x}S_2$ NSs play decisive roles in the fungicide process, suggesting their potential as a novel treatment method for fungal infection.

■ CONCLUSIONS

The work presented herein explores synthetic pathways to create novel nanomaterials with biological activity. The mixed metal chalcogenides $Mo_xRe_{1-x}S_2$ were formed via a hydrothermal synthesis method which generated flower-like nanostructures with uniform elemental distribution and maintained characteristics of MoS_2 and ReS_2 2D TMDCs. Detailed characterization of $Mo_xRe_{1-x}S_2$ NSs revealed a particle size range of 80−300 nm. The results of the present study revealed that the mixed-metals 2D chalcogenides $Mo_xRe_{1-x}S_2$ nanostructures, with the compositions $Mo_{0.66}Re_{0.34}S_{1.85}$ and $Mo_{0.81}Re_{0.19}S_{1.76}$, exhibit peroxidase-like behavior, qualifying them as nanozymes. The two compositions exert antifungal effects when tested on *C. albicans* in the presence of H_2O_2, which is characteristic of peroxidases. The antifungal testing was repeated in the presence of NIR irradiation to evaluate the enhancement of the antifungal effect, especially on localized applications. Antifungal tests demonstrated that the tested $Mo_xRe_{1-x}S_2$ materials exhibit excellent fungicidal properties in the presence of H_2O_2 when irradiated with an NIR laser. These findings suggest that $Mo_{0.66}Re_{0.34}S_{1.85}$ and $Mo_{0.81}Re_{0.19}S_{1.76}$ nanozymes could be further employed in fungicide development.

■ ASSOCIATED CONTENT

Supporting Information

The Supporting Information is available free of charge at https://pubs.acs.org/doi/10.1021/acsanm.4c05939.

> Chemical reagents for $Mo_xRe_{1-x}S_2$ Preparation; SEM EDX images of $Mo_xRe_{1-x}S_2$; zeta potential of $Mo_{0.66}Re_{0.34}S_{1.85}$ and $Mo_{0.81}Re_{0.19}S_{1.76}$; XRF elemental mapping for $Mo_{0.66}Re_{0.34}S_{1.85}$ and $Mo_{0.81}Re_{0.19}S_{1.76}$; particle size distribution of $Mo_{0.66}Re_{0.34}S_{1.85}$ and $Mo_{0.81}Re_{0.19}S_{1.76}$; preparation of pH solutions; photothermal conversion efficiency (η) of $Mo_xRe_{1-x}S_2$ NSs; plots of the steady-state kinetic assay of $Mo_{0.66}Re_{0.34}S_{1.85}$ and $Mo_{0.81}Re_{0.19}S_{1.76}$; kinetic parameters of the steady-state kinetic assay of $Mo_{0.66}Re_{0.34}S_{1.85}$ and $Mo_{0.81}Re_{0.19}S_{1.76}$; protocol of live/dead bacteria staining test (AO/PI); XRD of $Mo_{0.66}Re_{0.34}S_{1.85}$ synthesized with different reaction times; SEM EDX images of $Mo_{0.66}Re_{0.34}S_{1.85}$ at different reaction times; XRD patterns of $Mo_{0.66}Re_{0.34}S_{1.85}$ and $Mo_{0.81}Re_{0.19}S_{1.76}$ upon exposure under different pH solutions; photographs of the SDA agar plates with *C. albicans* following treatments at varying concentrations/pH (PDF)

■ AUTHOR INFORMATION

Corresponding Author

Cheng-Yu Lai − *Department of Mechanical and Materials Engineering, Florida International University, Miami, Florida 33174, United States; Department of Chemistry and Biochemistry, Florida International University, Miami, Florida 33199, United States;* orcid.org/0000-0002-8931-5601; Email: clai@fiu.edu

Authors

Fei Zhang − *Department of Mechanical and Materials Engineering, Florida International University, Miami, Florida 33174, United States*

Rishabh Sahani − *Department of Mechanical and Materials Engineering, Florida International University, Miami, Florida 33174, United States*

Changliang An − *Department of Mechanical and Materials Engineering, Florida International University, Miami, Florida 33174, United States*

Ha Na − *Department of Mechanical and Materials Engineering, Florida International University, Miami, Florida 33174, United States;* orcid.org/0000-0003-0872-7231

Samuel A. Oyon − *Department of Mechanical and Materials Engineering, Florida International University, Miami, Florida 33174, United States;* orcid.org/0009-0008-4519-663X

Daniela Radu − *Department of Mechanical and Materials Engineering, Florida International University, Miami, Florida 33174, United States;* orcid.org/0000-0001-6833-5825

Anthony J. McGoron − *Department of Biomedical Engineering, Florida International University, Miami, Florida 33199, United States;* orcid.org/0000-0003-3714-4676

Complete contact information is available at: https://pubs.acs.org/10.1021/acsanm.4c05939

Author Contributions

The manuscript was written through the contributions of all authors. All authors have approved the final version of the manuscript.

Notes

The authors declare no competing financial interest.

■ ACKNOWLEDGMENTS

This work was supported in part by the NSF Award DMR-2122078, NASA Award 80NSSC19M0201, USDA award USDA-2023-70410-41183, and DoD Awards W911NF2310152 and W911NF2210186. The authors thank Dr. Chen-Yu Chang for TEM imaging at FIU.

■ REFERENCES

(1) Bongomin, F.; Gago, S.; Oladele, R. O.; Denning, D. W. Global and Multi-National Prevalence of Fungal Diseases-Estimate Precision. *J. Fungi* **2017**, *3* (4), 57.

(2) Brown, G. D.; Denning, D. W.; Gow, N. A.; Levitz, S. M.; Netea, M. G.; White, T. C. Hidden Killers: Human Fungal Infections. *Sci. Transl Med.* **2012**, *4* (165), 165rv113.

(3) Lakemeyer, M.; Zhao, W.; Mandl, F. A.; Hammann, P.; Sieber, S. A. Thinking Outside the Box-Novel Antibacterials To Tackle the Resistance Crisis. *Angew. Chem., Int. Ed. Engl.* **2018**, *57* (44), 14440−14475.

(4) Guinea, J. Global Trends in the Distribution of *Candida* Species Causing Candidemia. *Clin Microbiol Infect* **2014**, *20* (s6), 5−10.

(5) Fan, F.; Liu, Y.; Liu, Y.; Lv, R.; Sun, W.; Ding, W.; Cai, Y.; Li, W.; Liu, X.; Qu, W. *Candida* albicans Biofilms: Antifungal Resistance, Immune Evasion, and Emerging Therapeutic Strategies. *Int. J. Antimicrob. Agents* **2022**, *60* (5−6), 106673.

(6) Perfect, J. R. The Antifungal Pipeline: a Reality Check. *Nat. Rev. Drug Discov* **2017**, *16* (9), 603−616.

(7) Sousa, F.; Ferreira, D.; Reis, S.; Costa, P. Current Insights on Antifungal Therapy: Novel Nanotechnology Approaches for Drug Delivery Systems and New Drugs from Natural Sources. *Pharmaceuticals* **2020**, *13* (9), 248.

(8) Francis, N.; Choudhary, Y. S.; Abraham, T.; Aravind, U. K.; Aravindakumar, C. T. TMDC-based Hybrid Photocatalyst for Antibiotics Degradation: A Comprehensive Review. *FlatChem.* **2024**, *45*, 100653.

(9) Manzeli, S.; Ovchinnikov, D.; Pasquier, D.; Yazyev, O. V.; Kis, A. 2D Transition Metal Dichalcogenides. *Nature Reviews Materials* **2017**, *2* (8), 1−15.

(10) Appel, J. H.; Li, D. O.; Podlevsky, J. D.; Debnath, A.; Green, A. A.; Wang, Q. H.; Chae, J. Low Cytotoxicity and Genotoxicity of Two-Dimensional MoS_2 and WS_2. *ACS Biomater Sci. Eng.* **2016**, *2* (3), 361−367.

(11) Na, H.; Venedicto, M.; Chang, C. Y.; Carrier, J.; Lai, C. Y. Infrared-Activated Bactericide: Rhenium Disulfide (ReS_2)-Functionalized Mesoporous Silica Nanoparticles. *ACS Appl. Bio Mater.* **2023**, *6* (4), 1577−1585.

(12) Everse, J. Heme Proteins. *Encyclopedia of Biological Chemistry*; Lennarz, W. J., Lane, M. D., Eds.; Elsevier, 2004; DOI: 10.1016/B0-12-443710-9/00304-5.

(13) Andrés, C. M. C.; Pérez de la Lastra, J. M.; Juan, C. A.; Plou, F. J.; Pérez-Lebeña, E. Chemistry of Hydrogen Peroxide Formation and Elimination in Mammalian Cells, and Its Role in Various Pathologies. *Stresses* **2022**, *2* (3), 256−274.

(14) Ye, Y.; Zou, J.; Wu, W.; Wang, Z.; Wen, S.; Liang, Z.; Liu, S.; Lin, Y.; Chen, X.; Luo, T.; et al. Advanced Nanozymes Possess Peroxidase-Like Catalytic Activities in Biomedical and Antibacterial Fields: Review and Progress. *Nanoscale* **2024**, *16* (7), 3324−3346.

(15) Cao, C.; Zhang, T.; Yang, N.; Niu, X.; Zhou, Z.; Wang, J.; Yang, D.; Chen, P.; Zhong, L.; Dong, X.; et al. POD Nanozyme Optimized by Charge Separation Engineering for Light/pH Activated Bacteria Catalytic/photodynamic Therapy. *Signal Transduct Target Ther* **2022**, *7* (1), 86.

(16) Yu, L.; Li, P. Investigation of Metal Nanoparticles Antibacterial Activity: Au@Pd Nanospheres against *Escherichia coli* and *Staphylococcus aureus*. *Journal of Food and Nutrition Research* **2023**, *11* (12), 737−741.

(17) Chen, T.; Zou, H.; Wu, X.; Liu, C.; Situ, B.; Zheng, L.; Yang, G. Nanozymatic Antioxidant System Based on MoS_2 Nanosheets. *ACS Appl. Mater. Interfaces* **2018**, *10* (15), 12453−12462.

(18) Zhang, X.; Wu, J.; Williams, G. R.; Niu, S.; Qian, Q.; Zhu, L. M. Functionalized MoS_2-Nanosheets for Targeted Drug Delivery and Chemo-Photothermal Therapy. *Colloids Surf. B Biointerfaces* **2019**, *173*, 101−108.

(19) Miao, Z. H.; Lv, L. X.; Li, K.; Liu, P. Y.; Li, Z.; Yang, H.; Zhao, Q.; Chang, M.; Zhen, L.; Xu, C. Y. Liquid Exfoliation of Colloidal Rhenium Disulfide Nanosheets as a Multifunctional Theranostic Agent for In Vivo Photoacoustic/CT Imaging and Photothermal Therapy. *Small* **2018**, *14* (14), 1703789.

(20) Presutti, D.; Agarwal, T.; Zarepour, A.; Celikkin, N.; Hooshmand, S.; Nayak, C.; Ghomi, M.; Zarrabi, A.; Costantini, M.; Behera, B.; et al. Transition Metal Dichalcogenides (TMDC)-Based Nanozymes for Biosensing and Therapeutic Applications. *Materials* **2022**, *15* (1), 337.

(21) Zou, J.; Zhang, X.; Xie, C.; Wei, A.; Zhao, Y.; He, Y.; Liu, Z.; Xu, J. Synthesis and characterization of 1T′ and 2H phase coexistence 2D $Re_{1-x}Mo_xS_2$ alloy films and their application for photodetectors. *Journal of Alloys and Compounds* **2024**, *993*, 174658.

(22) James, N.; Kini, S.; Pai, S.; Shenoy, N.; Kabekkodu, S. P. Comparative Evaluation of Corneal Storage Medias Used as Tooth Avulsion Medias in Maintaining the Viability of Periodontal Ligament Cells Using the Cell Counting Kit-8 Assay. *Clin Cosmet Investig Dent* **2022**, *14*, 87−94.

(23) Xu, B.; Li, S.; Zheng, L.; Liu, Y.; Han, A.; Zhang, J.; Huang, Z.; Xie, H.; Fan, K.; Gao, L.; et al. A Bioinspired Five-Coordinated Single-Atom Iron Nanozyme for Tumor Catalytic Therapy. *Adv. Mater.* **2022**, *34* (15), 2107088.

(24) Wang, X.; Shi, Q.; Zha, Z.; Zhu, D.; Zheng, L.; Shi, L.; Wei, X.; Lian, L.; Wu, K.; Cheng, L. Copper Single-atom Catalysts with Photothermal Performance and Enhanced Nanozyme Activity for Bacteria-Infected Wound Therapy. *Bioact Mater.* **2021**, *6* (12), 4389−4401.

(25) Taguchi, Y.; Hasumi, Y.; Abe, S.; Nishiyama, Y. The Effect of Cinnamaldehyde on the Growth and the Morphology of *Candida albicans*. *Med. Mol. Morphol* **2013**, *46* (1), 8−13.

(26) Deng, Q.; Li, X.; Si, H.; Hong, J.; Wang, S.; Feng, Q.; Hu, C. X.; Wang, S.; Zhang, H. L.; Suenaga, K.; et al. Strong Band Bowing Effects and Distinctive Optoelectronic Properties of 2H and 1T′ Phase-Tunable $Mo_xRe_{1-x}S_2$ Alloys. *Adv. Funct. Mater.* **2020**, *30* (34), 2003264.

(27) Sun, Q.; Mazumdar, D.; Yadgarov, L.; Rosentsveig, R.; Tenne, R.; Musfeldt, J. L. Spectroscopic Determination of Phonon Lifetimes in Rhenium-Doped MoS_2 Nanoparticles. *Nano Lett.* **2013**, *13* (6), 2803−2808.

(28) Al-Dulaimi, N.; Lewis, D. J.; Zhong, X. L.; Malik, M. A.; O'Brien, P. Chemical Vapour Deposition of Rhenium Disulfide and Rhenium-Doped Molybdenum Disulfide Thin Films Using Single-Source Precursors. *Journal of Materials Chemistry C* **2016**, *4* (12), 2312−2318.

(29) Rusciano, G.; Capaccio, A.; Sasso, A.; Singh, M.; Valadan, M.; Dell'Aversana, C.; Altucci, L.; Altucci, C. Single-Cell Photothermal Analysis Induced by MoS_2 Nanoparticles by Raman Spectroscopy. *Front Bioeng Biotechnol* **2022**, *10*, 844011.

(30) Kim, U.; Lee, S.; Koo, D.; Choi, Y.; Kim, H.; Son, E.; Baik, J. M.; Han, Y.; Park, H. Crystal Facet and Electronic Structure Modulation of Perovskite Oxides for Water Oxidation. *ACS Energy Letters* **2023**, *8* (3), 1575−1583.

(31) Tongay, S.; Sahin, H.; Ko, C.; Luce, A.; Fan, W.; Liu, K.; Zhou, J.; Huang, Y. S.; Ho, C. H.; Yan, J.; et al. Monolayer Behaviour in Bulk ReS_2 Due to Electronic and Vibrational Decoupling. *Nat. Commun.* **2014**, *5*, 3252.

(32) Lee, C.; Yan, H.; Brus, L. E.; Heinz, T. F.; Hone, J.; Ryu, S. Anomalous Lattice Vibrations of Single- and Few-Layer MoS_2. *ACS Nano* **2010**, *4* (5), 2695−2700.

(33) Tatur, S.; Maccarini, M.; Barker, R.; Nelson, A.; Fragneto, G. Effect of Functionalized Gold Nanoparticles on Floating Lipid Bilayers. *Langmuir* **2013**, *29* (22), 6606−6614.